

# Exploring Lattice Thermal Conductivity Models via Interpretable Deep Learning to Accelerate the Discovery of Novel Materials

Yuxuan Zeng,<sup>1</sup> Wei Cao,<sup>1,2,\*</sup> Yijing Zuo,<sup>2</sup> Tan Peng,<sup>2</sup> Yue Hou,<sup>3</sup> Ziyu Wang,<sup>1,2,4,†</sup> Ling Miao,<sup>5</sup> and Jing Shi<sup>2</sup>

<sup>1</sup>*The Institute of Technological Sciences, Wuhan University, Wuhan 430072, PR China*

<sup>2</sup>*Key Laboratory of Artificial Micro- and Nano-Structures of Ministry of Education, School of Physics and Technology, Wuhan University, Wuhan 430072, PR China*

<sup>3</sup>*The Institute of Technological Sciences, Wuhan University, 430072, PR China*

<sup>4</sup>*School of Physics and Microelectronics, Key Laboratory of Materials Physics of Ministry of Education, Zhengzhou University, Zhengzhou 450001, PR China*

<sup>5</sup>*School of Optical and Electronic Information, Huazhong University of Science and Technology, Wuhan 430072, PR China*

(Dated: February 4, 2025)

Lattice thermal conductivity, being integral to thermal transport properties, is indispensable to advancements in areas such as thermoelectric materials and thermal management. Traditional methods, such as Density Functional Theory and Molecular Dynamics, require significant computational resources, posing challenges to the high-throughput prediction of lattice thermal conductivity. Although AI-driven material science has achieved fruitful progress, the trade-off between accuracy and interpretability in machine learning continues to hinder further advancements. This study utilizes interpretable deep learning techniques to construct a rapid prediction framework that enables both qualitative assessments and quantitative predictions, accurately forecasting the thermal transport properties of three novel materials. Furthermore, interpretable deep learning offers analytically grounded physical models while integrating with sensitivity analysis to uncover deeper theoretical insights.

## I. INTRODUCTION

Lattice Thermal Conductivity (LTC) is a critical physical parameter that quantifies a material’s ability to transfer heat through lattice vibrations. It has diverse applications in thermal management [1], energy conversion [2], and thermoelectric materials [3]. High-LTC materials are used in electronic devices to efficiently dissipate heat and prevent overheating [4]. In contrast, low-LTC materials exhibit excellent performance in thermoelectric conversion, making them ideal for developing efficient thermoelectric generators (TEGs) [5] and coolers [6]. LTC is crucial for material design and optimization, yet acquiring it for specific materials is challenging.

Traditional experimental methods for measuring LTC, such as the laser flash method [7] and thermal conductivity probes [8], are often inefficient. In theoretical calculations, solving the Boltzmann Transport Equation (BTE) based on Density Functional Theory (DFT) is regarded as the most reliable method for determining LTC [9, 10]. Molecular Dynamics (MD) offers an alternative [11]; however, the former is limited by its substantial computational resource requirements, while the latter’s accuracy depends on the choice of interatomic potentials [12]. In recent years, machine learning (ML) has emerged as a powerful and efficient data mining tool, gaining widespread application in materials science [13]. The intersection of materials science and artificial intelligence is commonly referred to as “Materials Informatics” [14] or the “Materials Genome” [15]. Early ML-based predictions of material properties primarily aimed at achieving high prediction accuracy [16–18]. Nevertheless, such efforts, relying on “black-box” models, offered limited support for advancing

theoretical research in materials science. The focus has shifted towards model interpretability, prompting greater adoption of “white-box” models that contribute more substantially to theoretical advancements [19]. Research in materials informatics related to thermal conductivity has followed this trend. Efforts to predict LTC using black-box models such as Random Forest (RF) [20], Gaussian Process Regression (GPR) [21], and eXtreme Gradient Boosting (XGBoost) [22] have yielded reliable accuracy, whereas, the interpretability of these models is often hindered by their complexity. Alternatively, Genetic Programming-based Symbolic Regression (GPSR) [23] algorithms offer better interpretability, but their simplicity comes at the cost of reduced accuracy. The prevailing view is that the behavior and processes of complex models are difficult to understand and interpret, while simple models often lack strong fitting capabilities [19, 24, 25]. This presents a challenging trade-off, but the situation is gradually improving. The Sure Independence Screening and Sparsifying Operator (SISSO) [26], based on compressed sensing and symbolic regression, has not only surpassed the accuracy of the Slack semi-empirical model [27] but also narrowed the gap with black-box models like Kernel Ridge Regression (KRR) and GPR, and has been used to quantify feature sensitivity and identify key physical parameters influencing LTC [28]. Despite its potential, SISSO’s applicability is constrained by its high computational demands. Enumerating combinations of features and operators to construct descriptors poses an NP-hard problem [26], with resource requirements increasing for high-dimensional input features [29].

Kolmogorov-Arnold Networks (KANs) [30], a novel neural network architecture distinct from Multi-Layer Perceptrons (MLPs), show significant promise in solving partial differential equations (PDEs), time series prediction, and high-dimensional data tasks [30–32]. In some cases, smaller KAN models outperform MLPs [30, 31]. KANs have also demonstrated success in engineering applications, such as predict-

\* wei\_cao@whu.edu.cn

† zyuwang@whu.edu.cn

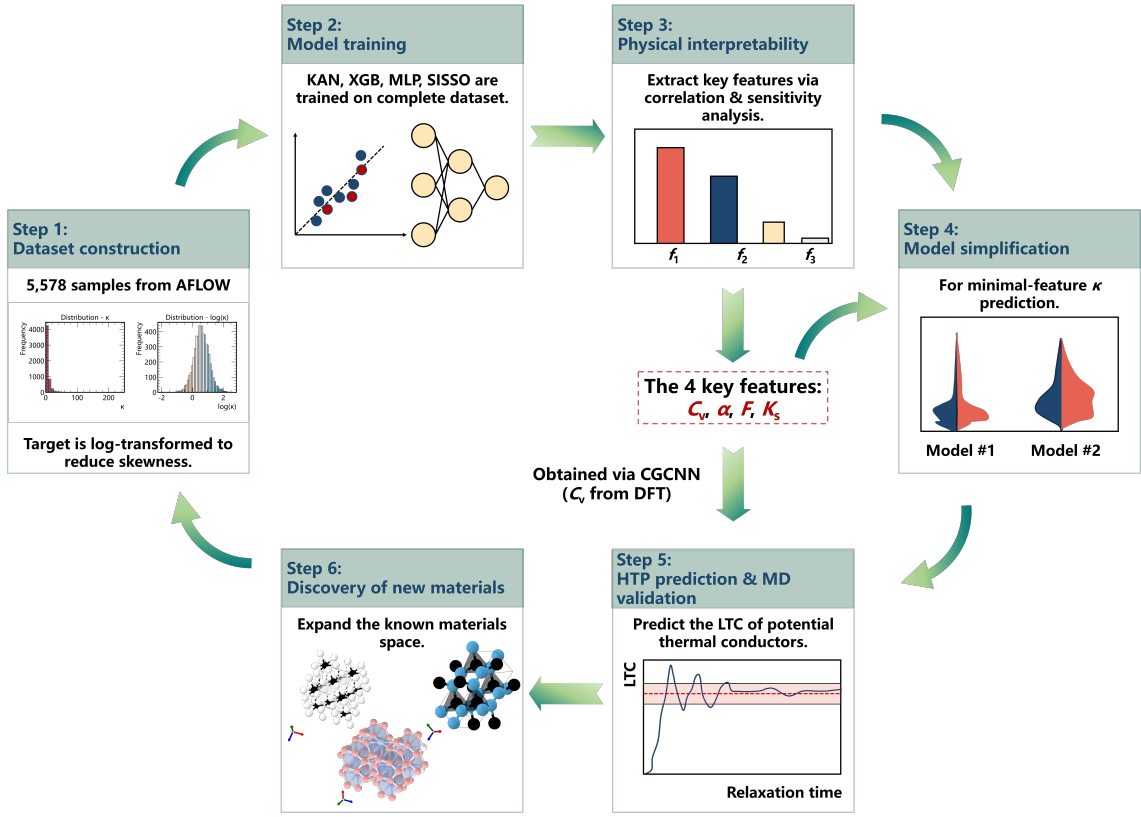


FIG. 1. A schematic illustration of the DL framework for LTC modeling and high-throughput prediction. This framework facilitates accurate and interpretable predictions of LTC for inorganic crystalline materials.

ing chiller energy consumption [33] and nuclear binding energy [34], highlighting both feasibility and broad potential. Notably, their capabilities in symbolic regression offer interpretability advantages absent in MLPs [30, 31]. As previously mentioned, existing work has successfully used black-box models to accurately predict LTC. However, achieving accurate LTC predictions while simultaneously visualizing the model’s decision-making process, akin to white-box model, remains a significant challenge. The emergence of KANs provides an opportunity to address this issue.

Figure 1 illustrates the framework of our work, which aims to model and predict LTC using the white-box deep learning model KAN and compare its performance with that of conventional black-box and white-box ML models. In addition to accuracy, we perform sensitivity analysis to examine interpretability differences across various white-box models and to assess the contributions of individual features to LTC. This approach further elucidates the relationships between LTC and key features, as well as feature-feature correlations. Additionally, Crystal Graph Convolutional Neural Network (CGCNN) [35] is employed to predict critical physical features required for LTC modeling with high accuracy, forming a two-stage framework that significantly reduces the time required for screening potential materials. This framework enables rapid qualitative assessments of thermal insulators and conductors. Finally, by integrating DFT and MD, our pretrained KAN model achieves outstanding accuracy in predicting the

properties of candidates in an unlabeled extrapolation dataset.

## II. RESULTS

### A. Establishment and evaluation of LTC models

TABLE I. The ranges for hyperparameter optimization.

Model	Hyperparameter	Range/Value
MLP	hidden_sizes	[64, 64, 64] (fixed)
	learning_rate	[0.001, 0.1]
	batch_size	[64, 256]
	num_epochs	[100, 600]
	n_estimators	[50, 500]
XGB	learning_rate	[0.0001, 0.5]
	max_depth	[1, 6]
	subsample	[0.8, 1]
	colsample_bytree	[0.8, 1]
	reg_alpha	[0.8, 1]
	reg_lambda	[5, 50]
KAN	width	[5, 15]
	grid	[5, 15]
	k	[2, 10]
	lamb.ll	[5, 50]
	steps	[20, 35]
	lr	[0.01, 1.0]

In selecting black-box models, we consider XGBoost and MLP as our primary options. XGBoost, a representative of ensemble learning, has demonstrated notable performance in various applications, including electrocaloric temperature change prediction in ceramics [17] and materials mechanical property prediction [36]. XGBoost is an enhancement of gradient boosting decision trees (GBDT). Compared to traditional GBDT, XGBoost introduces several innovations, including regularization (to improve generalization), a two-step gradient approximation for the objective function (to enhance computational efficiency), column subsampling (to reduce noise and boost generalization), and handling missing values (using a default direction for tree nodes, making it suitable for sparse datasets) [102]. MLP is a type of feedforward neural network consisting of an input layer, one or more hidden layers, and an output layer. Each neuron in a given layer is fully connected to all neurons in the preceding layer through weight matrices, allowing the network to perform linear combinations and nonlinear mappings of high-dimensional features. Neurons in each hidden layer typically use nonlinear activation functions such as ReLU, which endow the MLP with considerable expressive power, enabling it to approximate arbitrarily complex nonlinear functions. The training process of an MLP is carried out using the backpropagation algorithm, which optimizes the network’s weights through gradient descent to minimize a loss function. While MLPs exhibit substantial performance advantages in handling complex data patterns and feature learning tasks, their computational complexity and sensitivity to hyperparameter choices can make the training process time-consuming [38].

In our case, KAN was implemented using the `pykan-0.0.5` library ([github.com/KindXiaoming/pykan](https://github.com/KindXiaoming/pykan)), while MLP and XGBoost were built using the PyTorch [39] and `scikit-learn` [40] libraries, respectively. Initially, a trial-and-error approach was employed to determine approximate ranges for the hyperparameters that might yield good performance for KAN, MLP, and XGBoost. Subsequently, we employed the `Optuna` [41] library to perform automated hyperparameter optimization for these models. The task of identifying optimal hyperparameters for ML models can be conceptualized as finding the optimal solution to a multivariate optimization problem. It is crucial to acknowledge that hyperparameter optimization often converges to local optima rather than the global optimum, with achieving a global optimum remaining an inherently challenging endeavor. Within the hyperparameter space, multiple local optima may exist, and no algorithm can guarantee that the solution obtained is globally optimal [42]. Nevertheless, it is generally observed that with sufficient iterations, optimization algorithms often produce models with comparable performance across different hyperparameter configurations. This suggests that while achieving global optimality remains a complex challenge, practical implementations typically deliver satisfactory results within reasonable computational effort. The hyperparameter optimization ranges are detailed in Table I, while the final selected values are presented in Table S??.

In contrast to the previously discussed algorithms, SISSO imposes the highest computational demands during model

training. Therefore, we followed hyperparameter configurations recommended in established methodologies from related work [28]. To enhance interpretability, we maintained strict dimensional consistency across all features in SISSO, effectively eliminating any potential for invalid operations.

For regression models, the coefficient of determination ( $R^2$ ) provides more information compared to other commonly used criteria [43]. As shown in Figure 2(a), on the original dataset, XGB slightly outperforms KAN, which in turn outperforms MLP; however, the differences are marginal, and all three models are obviously better than SISSO. Additionally, SISSO exhibits severe errors in a very limited subset of samples with extremely low LTC values (approximately  $\log(\kappa) < -1$ ). This phenomenon indicates that SISSO struggles with datasets characterized by class imbalance. SISSO tends to fit more to samples with a higher frequency and a narrower range of target values when dealing with imbalanced data, leading to sub-optimal extrapolation performance. As a form of symbolic regression, SISSO inherently faces challenges in addressing sample imbalance. Common approaches to mitigate this issue in symbolic regression include resampling [44] and weighting [44, 45]. However, these methods inevitably impact the model’s interpretability [46, 47]. Therefore, we chose not to compromise SISSO’s interpretability solely for the purpose of enhancing its performance. It is noteworthy that XGBoost outperforms the deep learning models in this experiment, which can be attributed to several factors:

- Molecular features are often non-smooth, whereas deep models tend to favor smooth solutions [48, 49];
- Different dimensions of molecular features typically carry distinct information, yet deep models tend to integrate features across dimensions [49];
- Tree-based models like XGBoost inherently handle redundant features, while deep models are more susceptible to interference from such features [48];
- MLP is rotation-invariant, and any rotation-invariant learning process inherently exhibits the worst-case sample complexity [48].

In addition to accuracy, the symbolic models constructed by SISSO and KAN are also worth considering. The symbolic model provided by SISSO is as follows:

$$\log(\kappa)_{\text{SISSO}} = -2.8 + 0.3 \log \frac{\Theta^2}{|C_p - C_v|} - 0.17 \times 10^7 \gamma \mathcal{K}_1 \sqrt[3]{\Theta S_v} \quad (1)$$

the linear coefficients in the model are obtained through least-square regression. For the specific physical meanings of the features, please refer to Table II. Our dataset consists of a total of 10 features, but the SISSO model utilizes only seven of these. Some features, such as the space group number, which are typically not considered to be related to LTC. SISSO effectively identifies and excludes such extraneous variables. However, it overlooks physical quantities that are theoretically linked to LTC, such as the thermal expansion coefficient [50, 51]. Our feature sensitivity analysis indicates that

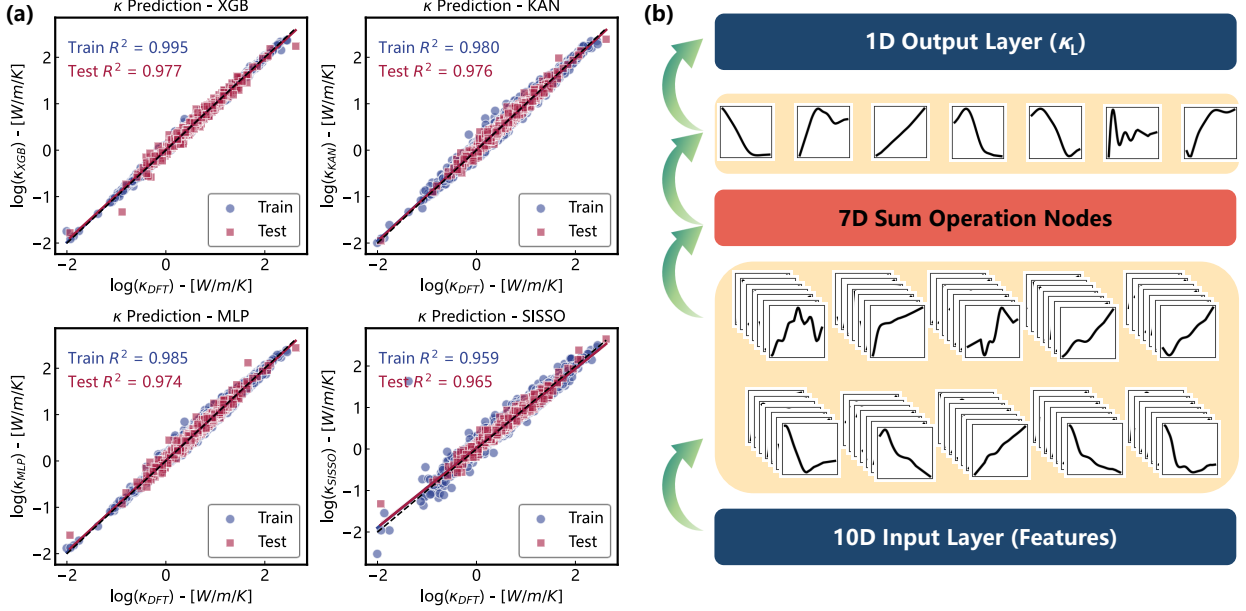


FIG. 2. Model performance on dataset with complete features. (a) The blue circular markers represent samples from the training set, while the red star scatters are samples from the test set. (b) KAN model architecture based on the original dataset.

the thermal expansion coefficient is regarded as an important parameter for modeling LTC. In this experiment, the network structure of the KAN model was also determined through automatic hyperparameter optimization via Optuna. The final architecture selected a dimensionality of 7 for the sum operation nodes (i.e., the network structure is  $10 \times 7 \times 1$ ), with one KAN layer preceding and another following this operation. In the first KAN layer, which connects to the input layer, there are  $10 \times 7 = 70$  residual activation functions, while in the second KAN layer, connected to the output layer, the number is  $7 \times 1 = 7$ . The detailed network architecture is shown in Figure 2(b). The MLP we designed features hidden layers with dimensions of  $64 \times 64 \times 64$ . This architecture balances robust pattern recognition capabilities and mitigating issues such as gradient explosion or vanishing gradients. Despite achieving comparable performance, KAN and MLP exhibit significant differences in terms of parameter count, with MLP generally requiring a substantially higher number of parameters. The analytical expressions provided by KAN are not equivalent to the model obtained through data training, unlike SISSO, where the resulting symbolic formula is exactly the model itself. In the KAN Layers, each residual activation function consists of a basis function and a linear combination of several B-spline functions. To symbolize the model, KAN selects the elementary functions with the highest linear correlation to the nodes as substitutes. After symbolization, KAN undergoes further training to determine the affine parameters for each symbolic function. Although this process enhances interpretability, it may slightly reduce performance. Nevertheless, in this experiment, the  $R^2$  value of the symbolic formula derived from

KAN, at 0.9655, remains higher than that obtained by SISSO. The symbolic model constructed by KAN is detailed in Supplementary Information Eq.( 1). The analytical expression derived by KAN is much more complex than that of SISSO, as each feature is involved in 7 operations, a consequence of the KAN architecture. Please note that each feature in this formula has undergone Min-Max normalization as part of the feature preprocessing. However, this preprocessing step does not affect the model’s interpretability, as it is easy to revert [52]. Despite the fact that the analytical expressions provided by KAN and SISSO accurately capture the relationship between features and LTC, there are a few points to consider:

- Generally, the symbolic models constructed through machine learning require more physical features (e.g., SISSO involves 7 features, while KAN utilizes all 10 features) compared to semi-empirical models (such as Slack [27], which, when the temperature variable is fixed at 300K, requires only 5 additional features). Moreover, obtaining the corresponding features for unknown materials often involves high experimental or computational costs, making such models appear less appealing at present.
- In materials inverse design, it is often necessary to regulate dominant features to induce changes in the target physical properties. Although the decision-making process of symbolic models is transparent, relying solely on the symbolic model itself to infer the dominance (or “contribution”) of different features is impractical.

TABLE II. Features adopted in the dataset.

Feature	Abbreviation	Explanation
space group relaxed	$SG$	The space group number for the relaxed structure
AGL Debye temperature	$\Theta$	Debye temperature
AGL Grüneisen parameter	$\gamma$	Grüneisen parameter
AGL heat capacity constant volume (300K)	$C_v$	Heat capacity per cell at constant volume (300K)
AGL heat capacity constant pressure (300K)	$C_p$	Heat capacity per cell at constant pressure (300K)
AGL thermal expansion coefficient (300K)	$\alpha$	Thermal expansion coefficient (300K)
AGL vibrational entropy atom (300K)	$S_v$	Vibrational entropy per atom (300K)
AGL vibrational free energy atom (300K)	$F$	Vibrational free energy per atom (300K)
AGL bulk modulus static (300K)	$K_s$	Static bulk modulus (300K)
AGL bulk modulus isothermal (300K)	$K_i$	Isothermal bulk modulus (300K)

- Both KAN and SISSO, as white-box models, achieve reliable predictive accuracy, but they differ in terms of interpretability. For instance, due to dimensional constraints (see Table S??), SISSO excludes certain features during model construction, and we cannot guarantee that the excluded features are necessarily redundant or useless. Similarly, in KAN, while different features have varying weights, we cannot ensure that all features genuinely influence LTC. Therefore, it is essential to introduce effective and robust quantitative methods to objectively evaluate the interpretability of these models.

### B. Deepening physical interpretability through sensitivity analysis

We identified the most critical features for LTC through two steps. The first step is correlation analysis, achieved by calculating correlation coefficients. The second step is sensitivity analysis, accomplished by computing sensitivity indices.

When constructing the dataset, we curated a selection of closely related features, such as heat capacity at constant volume ( $C_v$ ) and heat capacity at constant pressure ( $C_p$ ), as well as isothermal bulk modulus ( $K_i$ ) and static (adiabatic) bulk modulus ( $K_s$ ). The purpose of this approach was to ensure that the ML models achieve reliable accuracy. The correlation

coefficient heatmap can reveal the potential degree of linear association between features, as illustrated in Figure 3(a). It is important to clarify that  $K_i$  and  $K_s$  are not entirely identical concepts [53–55]. Both are temperature-dependent, and the difference between them increases as the temperature rises, but due to the minimal difference at 300K, a near-linear relationship appears, which is also observed between the two specific heat capacities [53]. Interestingly, in addition to the previously mentioned bulk moduli and heat capacities, the Debye temperature  $\Theta$ , vibrational free energy per atom  $F$ , and vibrational entropy per atom  $S_v$  also show a high degree of linear correlation. The quantitative relationship between vibrational free energy and vibrational entropy is defined by the following equation [56]:

$$F = Q - TS_v \quad (2)$$

where  $Q$  represents the total enthalpy of formation of the compound, denotes Kelvin temperature (here  $T = 300K$ ), and the equation above can be rewritten as  $\frac{F}{S_v} = \frac{Q}{S_v} - T$ . Due to the presence of the entropy-enthalpy compensation (EEC) [57] effect, a linear relationship exists between entropy and enthalpy, which is further reflected in the linear correlation between  $S_v$  and  $F$ . Based on the work of G. D. Garbulsky and G. Ceder [58], within the harmonic approximation, when the temperature is greater than the system’s characteristic Debye temperature, the lattice Hamiltonian can be written as:

$$H(\vec{\sigma}, T) = E_0(\vec{\sigma}) + \langle \ln(\omega) \rangle(\sigma) k_B T + \frac{\hbar \langle \omega^2 \rangle(\vec{\sigma})}{24k_B T} - \frac{\hbar^4 \langle \omega^4 \rangle(\vec{\sigma})}{2880k_B^3 T^3} + \dots \quad (3)$$

where the  $\vec{\sigma}$  denotes the configuration of  $A$  and  $B$  atoms on the lattice, while  $\langle \rangle$  represents the average operation (per atom) over the Brillouin zone.  $E_0$  refers to the fully relaxed ground state energy,  $\omega$  is the vibrational frequency of a phonon mode,  $k_B$  and  $\hbar$  correspond to the Boltzmann and Planck constants, respectively. As the temperature approaches the Debye temperature, setting  $T = \Theta$ , we have:

$$F \approx \langle \ln(\omega) \rangle(\sigma) k_B T \quad (4)$$

where  $\langle \ln(\omega) \rangle(\sigma)$  is a constant, thus the vibrational free energy per atom is approximately linearly related to the Debye temperature [58]. These conclusions, combined with Eq.(4) sufficient explanation for the linear relationship between  $\Theta$ ,  $F$ , and  $S_v$ .

We propose that among highly linearly correlated physical features, retaining only one is sufficient. Under ideal conditions, this approach can simplify the ML model without significantly degrading its performance. To achieve this goal,

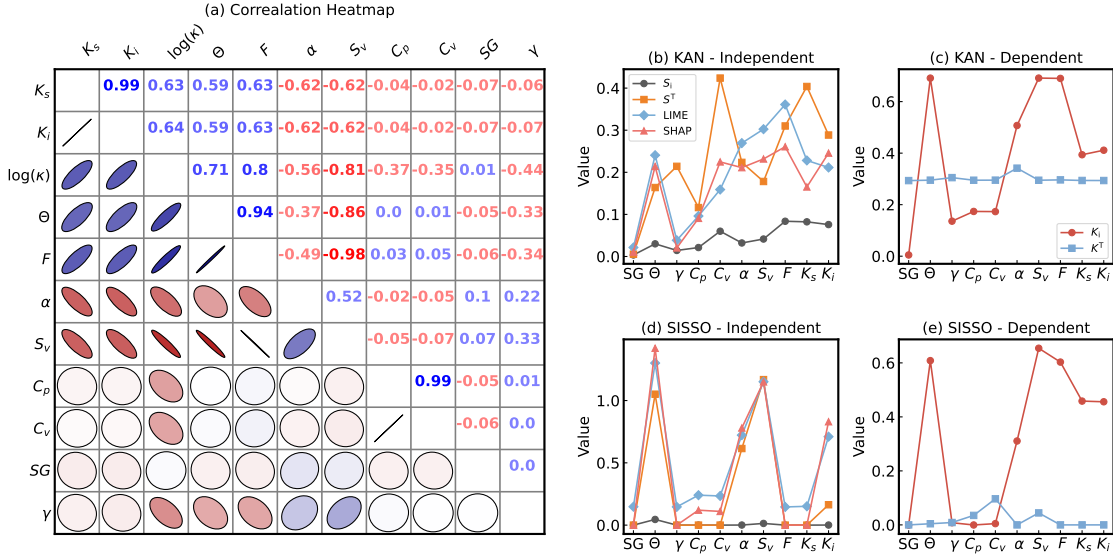


FIG. 3. Feature correlation and sensitivity analysis. (a) A heatmap of correlation coefficients is presented, where the numbers in the upper-right triangle represent the Pearson correlation coefficients between pairs of features. In the lower-left triangle, the direction of the ellipse’s long axis indicates the positive or negative correlation, while the area reflects the strength of correlation. (b)–(e) Different sensitivity analysis methods are applied to evaluate feature importance for both the KAN and SISSO models.

it is necessary to combine correlation analysis with sensitivity analysis. The purpose of sensitivity analysis is to determine which features have a greater impact on the target compared to others, or, more simply, which features are more “important” for the target. Currently, mainstream sensitivity analysis algorithms include SHAP [105], LIME [60], and Sobol [61]. However, these methods generally assume feature independence and the features used in our work are interdependent, their applicability is limited. Ignoring input interactions and multivariate distribution characteristics can severely skew or even invalidate any sensitivity analysis results [62]. Kucherenko et al. [63] improved the traditional Sobol index by using Copula-based sampling to separate each feature’s marginal and joint distributions, thereby constructing a dependency model. In this work, we will implement the Kucherenko indices using UQLab [64] and compare it with other indices.

As shown in Figure 3, we calculated the mean absolute values of various sensitivity indices, which provide the global values for SHAP and LIME. It is important to note that, regardless of the white-box machine learning surrogate model used, results obtained under the assumption of feature independence lack persuasiveness. In Figure 3(b), significant differences exist among the results from different methods, making it difficult to determine which is more reliable. In Figure 3(d), although different analysis methods yield similar feature sensitivities, correlated features should exhibit similar sensitivities [65]. Evidently, the conclusions from Figure 3(b) and (d) do not satisfy this premise. Therefore, conclusions drawn from sensitivity analysis methods that ignore feature interaction effects lack credibility.

The sensitivity analysis results in Figure 3(c) and (e) are

relatively reasonable and satisfy the premise of “similar sensitivities for correlated features,” but differences still exist. For instance, in Figure 3(e), the total effect indices of  $C_p$  and  $C_v$  are higher than those of other features, yet their first-order effect indices are approximately zero. A total effect index slightly higher than the first-order effect index indicates that the independent contributions of the features themselves are minimal, but their combinations with other features exert additional influence on the model output. In the symbolic SISSO model (Eq. 1), specific heat capacities appear in the form  $|C_v - C_p|$ . Such interaction terms reduce the contribution of individual specific heat variables but result in a higher total contribution. However, a first-order effect index of zero suggests that  $\log(\kappa)$  is entirely independent of specific heat capacities.

When considering empirical models like Slack’s, the sensitivity analysis results of the SISSO symbolic model are contradictory and unsustainable, as they underestimate the influence of specific heat capacities on  $\log(\kappa)$ . Furthermore, despite the presence of other highly correlated variables, the removal of redundant features causes a noticeable performance degradation in the SISSO model, as shown in Figure 4(a). This indicates that SISSO fails to accurately capture the correlations between physical quantities and exhibits poor robustness, whereas the KAN model shows the opposite behavior. For a primary feature, a  $K_i$  value exceeding  $K^T$  indicates a strong correlation with other features, while  $K^T = 0$  signifies an exact correlation with other inputs [28, 66]. From this perspective, KAN is more effective than SISSO at overcoming feature dependency. This advantage can be attributed to KAN’s neural network architecture. As illustrated in Figure 4(b), in the absence of pruning, the neurons in KAN’s hidden layers are fully con-

nected to both preceding and subsequent layers. This design allows each feature to independently and equitably contribute to  $\log(\kappa)$ . Simultaneously, KAN leverages backpropagation to update the weights of various nodes, ensuring the model achieves optimal accuracy. This process not only guarantees fair participation of all features in model training but also effectively distinguishes their relative contribution.

Ultimately, we retained  $C_v$ ,  $\alpha$ ,  $F$ , and  $K_s$  as the features for the reduced dataset, as these features preserve as much of the original information as possible while enabling fast and accurate predictions via CGCNN, thereby facilitating high-throughput screening of new materials. As shown in Figure 4(a), the four selected features are sufficient to describe the physical mechanism of LTC with a high degree of confidence.

Similar to other black-box models, KAN exhibits only a negligible decline in performance with the reduction in feature count. In contrast, SISSO's performance deteriorates significantly. This decline is likely due to the complexity constraints of the SISSO model. In contrast to KAN, SISSO is characterized by a relatively limited number of operators (see Eq.13), and its descriptors typically have a dimensionality of no more than 3. Exceeding this limit would lead to much greater computational resource demands compared to KAN and black-box models. These complexity constraints limit SISSO's expressive capacity and hinder its ability to capture complex physical feature-mapping relationships.

After key feature extraction, we performed symbolic regression again using KAN and SISSO. The symbolic model fitted by KAN became considerably simplified, as shown below:

$$\log(\kappa)_{\text{KAN}} = -1.05 \sin f_1(F, K_s, \alpha, C_v) + 0.61 \cosh f_2(F, K_s, \alpha, C_v) - 1.44 + 1.4e^{-19.72f_3^2(F, K_s, \alpha, C_v)} - 0.48e^{-63.21f_4^2(C_v, K_s, F)} \quad (5)$$

where

$$\begin{aligned} f_1(F, K_s, \alpha, C_v) &= -5.66(0.77 - F)^2 - 0.7 \tan(1.56K_s - 4.4) + 2.89 + 1.56e^{-13.65(-\alpha - 0.17)^2} + 0.85e^{-26.37(-C_v - 0.11)^2}, \\ f_2(F, K_s, \alpha, C_v) &= -0.76 \sin(4.23F + 4.79) + 1.03 \tan(1.55\alpha - 0.99) - 0.86 \cosh(5.35C_v - 1.75) \\ &\quad + 0.38 \operatorname{atan}(8.56K_s - 0.63) + 2.31, \\ f_3(F, K_s, \alpha, C_v) &= (0.38 - K_s)^3 - 0.09 \sin(6.2C_v - 6.16) - 0.08 \operatorname{atan}(4.8F - 1.66) + 0.47 - 0.26e^{-38.44(-\alpha - 0.06)^2}, \\ f_4(C_v, K_s, F) &= -(0.37 - C_v)^2 - 0.13 \tan(1.46K_s - 0.63) - 0.3 + 0.28e^{-2.53(-F - 0.02)^2}. \end{aligned}$$

The analytical expression fitted by SISSO remains consistently concise:

$$\log(\kappa)_{\text{SISSO}} = 1.53 + 0.0079 \frac{F \log(C_v)}{\sqrt[3]{C_v}} - 45.57 \sqrt[3]{\alpha^2 C_v K_s} \quad (6)$$

Following feature reduction, the  $R^2$  of the analytical expression derived by KAN was 0.9639, exhibiting minimal degradation in accuracy compared to its pre-reduction value of 0.9655. In contrast, as illustrated in Figure 4(a), SISSO experienced a pronounced decline in accuracy. Consequently, we assert that KAN more effectively captures the mapping relationship between LTC and the features, while also demonstrating exceptional robustness.

### C. Screening potential thermal insulators/conductors

Unlike simple descriptors that can be directly generated by programs, such as those based on composition (e.g., Mag-

pie [67]) or structure (e.g., Coulomb matrix [68]), the physical features involved in the aforementioned reduced dataset are relatively complex and not easily constructed physical quantities. Inspired by previous studies [69, 70], our approach is to use a two-stage prediction method. We predict features by simple descriptors and models, and then use the predicted features to perform high-throughput predictions of the LTC for unknown materials. CGCNNs have achieved accuracy comparable to or even surpassing DFT in predicting energy-related and mechanical properties [35]. In our application, CGCNNs delivered fairly accurate results for the prediction of all features except for  $C_v$ , where the prediction accuracy was notably lower (see Supplementary Information for details). Therefore, we focus on first screening a subset of potential thermal insulating/conductive materials using features that can be reliably predicted qualitatively, and then calculating  $C_v$  using DFT. This approach is more efficient than directly using DFT or MD methods to calculate LTC.

Based on the information from Figure 3(a) and Figure 5(a)-(d), it can be concluded that  $F$ ,  $K_s$ , and  $\kappa$  exhibit a strong pos-

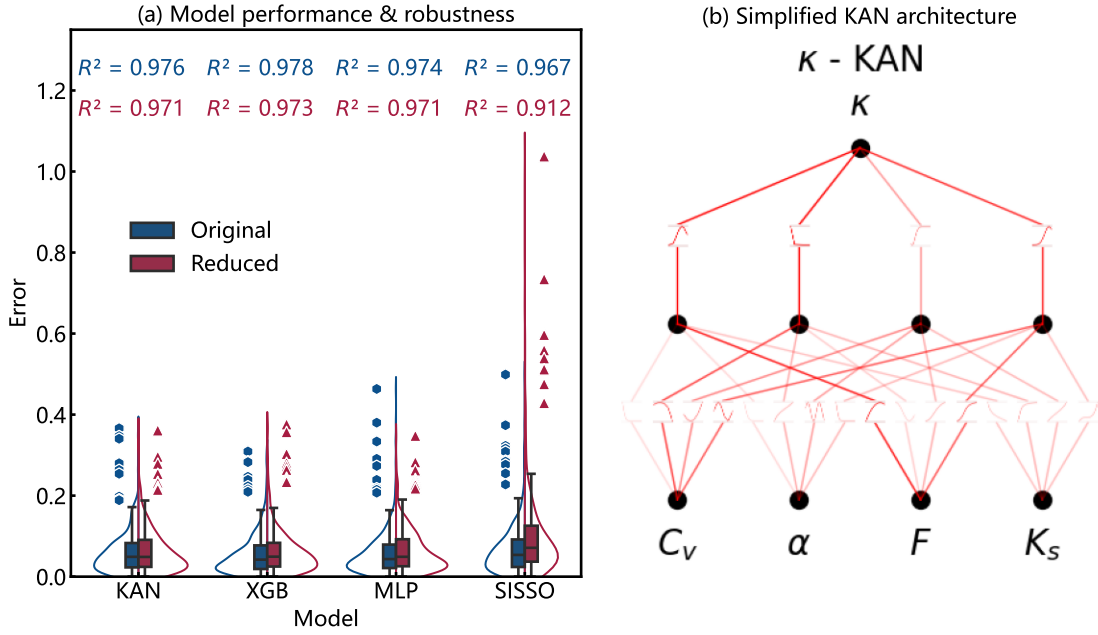


FIG. 4. Performance comparison before and after dimensionality reduction. (a) After extracting key features and re-modeling the LTC, both KAN and the black-box models exhibited good robustness, while the robustness of SISSO did not meet expectations. (b) The simplified architecture of KAN model.

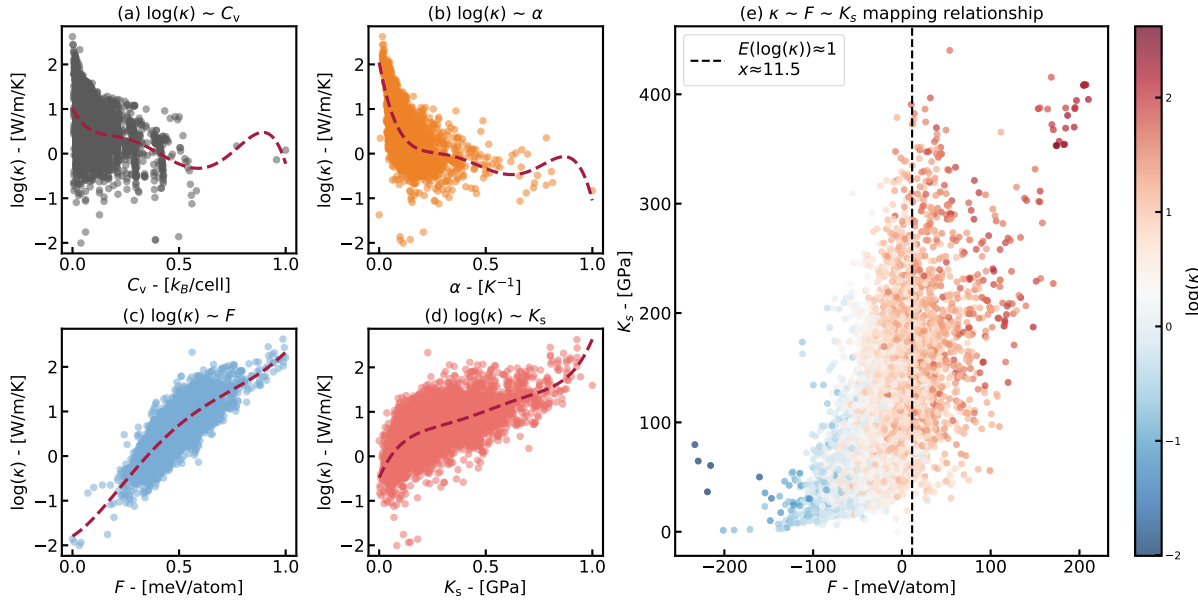


FIG. 5. Correlation between the 4 features and LTC. (a)-(d) The two-dimensional mapping of different features with  $\log(\kappa)$ , where the color bar reflects the scatter density, and the feature values have been min-max normalized. (e) The mapping between  $\log(\kappa)$  and  $F$ ,  $K_s$ , with the color bar indicating the  $\log(\kappa)$  of each sample. The dashed line represents the mean  $\log(\kappa)$  value of 1 for the samples.

itive linear correlation. Materials with higher  $F$  and  $K_s$  values generally exhibit higher LTC, a relationship that is further confirmed in Figure 5(e). Therefore, the preliminary qualitative screening of thermal insulators and conductors based on  $F$  and  $K_s$  is highly beneficial for accelerating the exploration of new

materials. The predictions of  $F$  and  $K_s$  using CGCNN are shown in Figure 6(a) and 6(b), with  $R^2$  values reaching 0.94 and 0.98, respectively. We extracted a total of 2,246 samples from the Materials Project [71] with the following selection criteria:

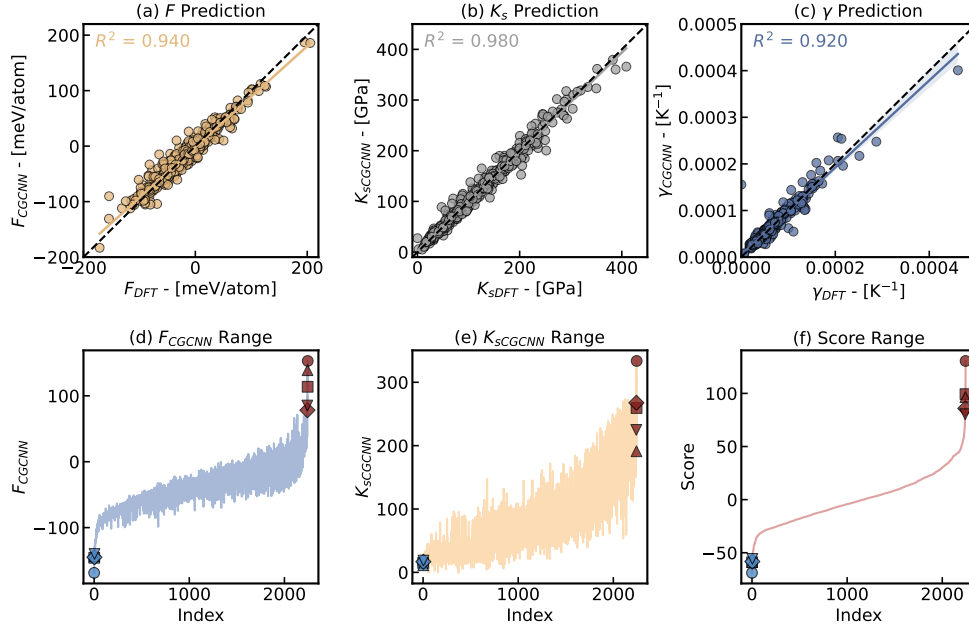


FIG. 6. Using CGCNN to predict key features and qualitatively assess LTC. (a), (b), and (c) display scatter plots comparing the CGCNN-predicted values of three features with the DFT-calculated values on their respective test sets. (d), (e), and (f) illustrate the distribution curves of  $F$ ,  $K_s$ , and scores for Materials Project samples, ordered by their comprehensive scores, with the red and blue scatter points of varying shapes representing the top 5 and bottom 5 samples, respectively.

- Excluding transition metal elements;
- Number of atoms ( $n_{sites}$ ) < 5;
- Band gap  $\in (0, 1.5\text{eV}]$

Additionally, we developed a comprehensive score to qualitatively evaluate a sample's potential to become a thermal insulator or conductor. This score incorporates the linear coefficients between features and targets, the Kucherenko indices of features with respect to the target, and the features themselves:

$$\text{Score} = \frac{K_F}{K_F + K_{K_s}} \frac{R_F}{R_F + R_{K_s}} F + \frac{K_{K_s}}{K_F + K_{K_s}} \frac{R_{K_s}}{R_F + R_{K_s}} K_s \quad (7)$$

where  $K$  represents the respective Kucherenko index, and  $R$  denotes the Pearson correlation coefficient. Based on the scores of the materials, we retained the top 5 and bottom 5 samples to verify their potential as thermal conductors or insulators. Existing literature [72–77] on these samples primarily focuses on 2D materials or electronic thermal conductivity. In contrast, our research targets the LTC of 3D materials, aiming to fill this gap in the field.

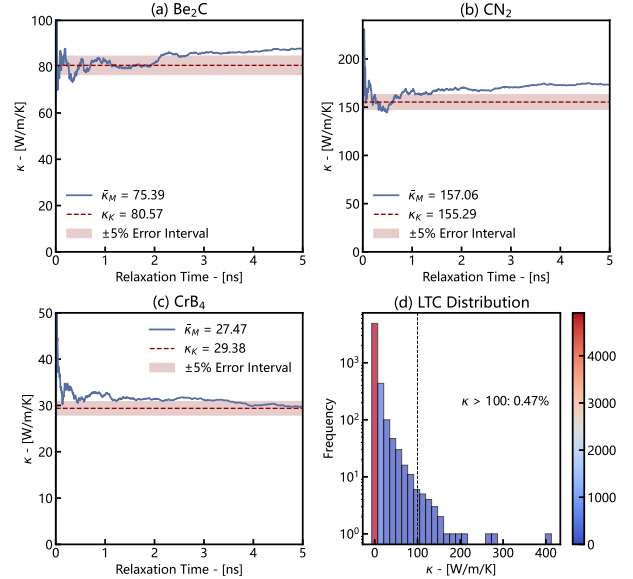


FIG. 7. Validation of the KAN predictions. For (a)  $\text{Be}_2\text{C}$ , (b)  $\text{CN}_2$  and (c)  $\text{CrB}_4$ , a relaxation time of 5 ns is sufficient for the thermal conductivity to converge. The deep red dashed line represents the thermal conductivity predicted by the KAN model, while the light red band indicates the prediction range with a  $\pm 5\%$  error margin. The LTC calculated by MD is represented by the blue line, illustrating its convergence behavior with respect to relaxation time. (d) shows a histogram of the thermal conductivity distribution in the original dataset.

Based on the conclusions provided by the MP database, most of the 10 selected structures are predicted to be unstable; consequently, only a few materials, such as  $\text{CN}_2$ ,  $\text{Be}_2\text{C}$ ,  $\text{CrB}_4$ ,  $\text{CuBO}_2$ , and  $\text{BeSiO}_3$ , possess valid  $C_v$  values obtained through DFT calculations (see Table III). We utilized GPUMD to calculate both the surface and bulk thermal conductivities of viable candidate materials. For isotropic crystals, we computed results in only one direction. For anisotropic crystals, we calculated the LTC in each direction and averaged these values to represent the overall performance. Notably,  $\text{CN}_2$  exhibits thermal conductivity exclusively in the  $z$ -direction. As such, averaging the LTC across multiple directions for this material is not meaningful, and the  $z$ -direction thermal conductivity is used to represent its overall performance. Figure 7(a), (b), and (c) illustrate the LTC convergence for each material. We calculated both the surface and bulk thermal conductivities of each material over relaxation times ranging from 0 to 10 ns, providing the sum of these values for comparison with the predictions from the KAN model. In our work, the pretraining model faced several challenges:

- **Feature selection:** Initially, the original dataset provided 10-dimensional features for training all models. However, to reduce model complexity, enhance interpretability, and account for the difficulty of obtaining certain features, we applied sensitivity analysis to narrow the features down to just four dimensions. While both KAN and the black-box models demonstrated remarkable robustness, the uncertainty introduced by feature selection remains a consideration.
- **Two-stage prediction:** As shown in Figure 6, three features for the candidate materials were derived from CGCNN predictions, with only  $C_v$  obtained from DFT calculations. Although CGCNN and DFT provide satisfactory accuracy for individual properties, the two-stage prediction process inevitably introduces cumulative errors in predicting the LTC of candidate materials.
- **Data imbalance [78]:** As depicted in Figure 7(d), only 0.47% of the samples in the dataset used for model pretraining have an LTC > 100 W/m/K. Consequently, the model tends to favor the more abundant low- and medium-conductivity materials, potentially limiting its extrapolation capability in unrepresented regions.

According to our MD calculations, the candidate materials exhibit LTC values within distinct ranges (30, 80, 150 W/m/K). Despite this, their ML-predicted LTC consistently align with expectations. This demonstrates that the pretrained KAN model achieves not only reliable accuracy but also satisfactory extrapolation capability. Although the qualitative scores for  $\text{CrB}_4$  and  $\text{Be}_2\text{C}$  are quite close, there is a significant difference in their actual thermal conductivities. This discrepancy is attributed to a notable difference in their heat capacities (see Table III), which is not accounted for in Eq. 6 due to its negligible negative correlation with LTC. However, overall, the qualitative assessment method in this study helped us identify other new materials with excellent thermal conduc-

tivity, and it proved valuable in improving the efficiency of material screening.

### III. DISCUSSION

In the past, researchers often relied on empirical or semi-empirical models to calculate the LTC of materials. However, as the range of explored materials continues to expand, the inaccuracies inherent in empirical models have become increasingly problematic. Machine learning-based LTC modeling has achieved remarkable accuracy, but improvements in accuracy alone offers limited contributions to the advancement of materials science. Black-box models, such as neural networks and ensemble learning, excel in accuracy but their complex structures hinder the understanding of feature-target relationships. In contrast, white-box models like symbolic regression provide transparent structures, making their internal mechanisms interpretable, but this often comes at the cost of accuracy. Traditionally, the interpretability and accuracy of ML or DL models have been seen as mutually exclusive, akin to “having your cake and eating it too.” However, in the context of LTC modeling, interpretable DL models like KAN have demonstrated significant success in balancing both accuracy and interpretability.

In this study, we employed KAN to model LTC, demonstrating that its performance in terms of both accuracy and robustness is fully comparable to that of black-box models. For the interpretability analysis of white-box models, we considered feature interaction effects. Sensitivity analysis results based on the KAN and SISO models revealed that KAN can accurately extract key features, highlighting its superior interpretability in this context. Additionally, the analytical expressions derived from KAN serve as a valuable supplement to traditional empirical models. We also developed a two-stage high-throughput prediction framework, integrating CGCNN to accurately predict the primary physical features required for LTC. For  $C_v$ , a property that CGCNN cannot predict accurately, DFT calculations were used. Building on this foundation, the predictions from the KAN pretraining model aligned closely with MD validation results, enabling us to successfully identify three new materials, one of which was confirmed as an excellent thermal conductor. Compared to using MD to directly compute LTC for unknown materials, our high-throughput prediction framework requires only DFT calculations of  $C_v$  to achieve MD-level predictive accuracy. This work not only accelerates the prediction of material thermal conductivity but also enhances our understanding of the underlying physical mechanisms. By balancing accuracy and interpretability, KAN demonstrates its potential as a powerful tool for advancing materials informatics.

TABLE III. The predicted results of LTC based on KAN.

MPID	Formula	$F_{pred}$	$K_s-pred$	$\gamma_{pred}$	$C_v-DFT$	$\kappa_{KAN}$
mp-1009818	CN <sub>2</sub>	152.8788	333.6628	$1.71^{-5}$	0.2343	155.2907
mp-27710	CrB <sub>4</sub>	113.7286	259.3992	$2.73^{-5}$	12.7181	29.3775
mp-1569	Be <sub>2</sub> C	138.8222	191.1319	$2.41^{-5}$	4.6692	80.5562
mp-1096940	CuBO <sub>2</sub>	78.15269	267.6422	$3.04^{-5}$	8.4535	31.3254
mp-1183445	BeSiO <sub>3</sub>	85.25379	224.8873	$2.56^{-5}$	9.5514	41.3833
mp-1095948	Cs <sub>2</sub> KNa	-139.976	18.569	/	/	/
mp-1097263	Cs <sub>2</sub> RbNa	-144.966	16.8264	/	/	/
mp-10378	Cs <sub>3</sub> Sb	-143.5	11.2367	/	/	/
mp-1097633	Cs <sub>2</sub> KRb	-145.791	14.89677	/	/	/
mp-635413	Cs <sub>3</sub> Bi	-168.671	13.74844	/	/	/

## IV. METHODS

### A. Kolmogorov-Arnold Networks (KANs)

The Kolmogorov-Arnold representation theorem [79] provides that any multivariate continuous function defined on a bounded domain can be expressed as a finite composition of continuous functions of a single variable, combined with the operation of addition [80]. For a differentiable function  $f : [0, 1]^n \rightarrow \mathbb{R}$ :

$$f(\mathbf{x}) = f(x_1, \dots, x_n) = \sum_{q=1}^{2n+1} \Phi_q \left( \sum_{p=1}^n \phi_{q,p}(x_p) \right) \quad (8)$$

where  $\phi_{q,p} : [0, 1] \rightarrow \mathbb{R}$  as well as  $\Phi_q : \mathbb{R} \rightarrow \mathbb{R}$ . In this

context,  $p$  denotes the number of top operators,  $q$  denotes the number of bottom operators, and  $n$  denotes the number of nodes in the bottom network (which corresponds to the dimensionality of the input features in the input layer),  $\mathbf{x} = (x_1, \dots, x_n)$  represents feature vector.

In the original K-A representation theorem, the number of nonlinear layers is limited to 2, and the number of hidden layer nodes is set to  $2n + 1$ , which fixes the network structure to  $[n, 2n + 1, 1]$ . However, Liu et al. [30] are not constrained by these limitations. In KANs, both the number of layers and the width of the network are arbitrary, which enhances the feasibility of the K-A representation theorem for ML applications. Therefore, for a KAN with  $n_0$ -D inputs,  $L$  layers, and  $n_L = 1$ -D output, a more precise definition is:

$$\text{KAN}(\mathbf{x}) = \sum_{i_{L-1}=1}^{n_{L-1}} \phi_{L-1, i_L, i_{L-1}} \left( \sum_{i_{L-2}=1}^{n_{L-2}} \cdots \left( \sum_{i_2=1}^{n_2} \phi_{2, i_3, i_2} \left( \sum_{i_1=1}^{n_1} \phi_{1, i_2, i_1} \sum_{i_0=1}^{n_0} \phi_{0, i_1, i_0}(x_{i_0}) \right) \right) \cdots \right) \quad (9)$$

the expression can be simplified to:

$$\text{KAN}(\mathbf{x}) = (\Phi_{L-1} \circ \Phi_{L-2} \circ \cdots \circ \Phi_1 \circ \Phi_0) \mathbf{x} \quad (10)$$

in the expression,  $\Phi_i = \{\phi_{q,p}\}$  denotes the  $i$ -th layer of the KAN, defined as a tensor of 1-D activation functions  $\phi_{q,p}$ . In the implementation details,  $\phi(x)$  is represented as a linear combination of the basis function  $b(x)$  and B-spline function:

$$\phi(x) = \omega [b(x) + \text{spline}(x)] = \omega \left[ \frac{x}{1 + e^{-x}} + \sum_i c_i B_i(x) \right] \quad (11)$$

where B-spline function is defined as:

$$B_{i,0}(x) = \begin{cases} 1, & \text{if } t_i \leq x < t_{i+1}, \\ 0, & \text{otherwise.} \end{cases}$$

$$B_{i,k}(x) = \frac{x - t_i}{t_{i+k} - t_i} B_{i,k-1}(x) + \frac{t_{i+k+1} - x}{t_{i+k+1} - t_{i+1}} B_{i+1,k-1}(x). \quad (12)$$

In KANs, the coefficients  $c$ , the degree  $k$ , and the grid  $G$  of the spline functions are all learnable parameters, which are updated through backpropagation.

### B. Sure Independence Screening & Sparsifying Operator (SISSO)

SISSO constructs a descriptor vector  $\mathbf{d}_n$  using features and operators, and models the target vector  $\mathbf{P}$  through a linear combination of  $n$ -dimensional descriptors. The initial feature  $\Phi_0$  serves as the starting point for constructing descriptors and includes easily obtainable physical parameters. The operator set is defined as:

$$\hat{H}^{(m)} \equiv \{I, +, -, \times, \div, \exp, \log, \text{abs}, \sqrt{\cdot}, ^{-1}, ^{-2}, ^{-3}\} [\phi_1, \phi_2] \quad (13)$$

where  $\phi_1$  as well as  $\phi_2$  are terms in  $\Phi_i$ . The superscript  $^{(m)}$  indicates that SISSO retains only descriptors with physical

meaning. For example, features that are added or subtracted must have the same dimensions, and features involved in logarithmic or square root operations cannot be negative. The new features constructed during the  $i$ -th iteration can be expressed as

$$\Phi_i = \bigcup_k \hat{h}_k^{(m)} [\hat{\phi}_i, \hat{\phi}_j], \forall \hat{h}_k^{(m)} \in \hat{H}^{(m)} \text{ and } \forall \phi_i, \phi_j \in \Phi_{i-1} \quad (14)$$

where  $\hat{h}_k^{(m)}$  represents single operator of  $\hat{H}^{(m)}$ ,  $\phi_i$  and  $\phi_j$  are different elements from  $\Phi_{i-1}$ . SIS [81] constructs the feature subspace with the highest correlation to the target  $\mathbf{P}$  through vector inner products, while SO selects the top  $n$  features with the highest relevance using regularization techniques to form the descriptor matrix  $\mathbf{d}_n$ . The linear coefficients can be approximately determined by solving the equation  $\mathbf{c}_n = (\mathbf{d}_n^T \mathbf{d}_n)^{-1} \mathbf{d}_n^T \mathbf{P}$ , so the model constructed by SISSO can be represented as:

$$\hat{\mathbf{P}} = \mathbf{d}_n \mathbf{c}_n = c_0 + c_1 d_1 + \dots + c_n d_n \quad (15)$$

where  $\hat{\mathbf{P}}$  represents the estimated target vector of the model.

### C. Sobol Indices

Sobol is a method for feature importance analysis based on analysis of variance (ANOVA) [61]. It allocates a portion of the total variance to each input variable or its interactions with other variables, thereby providing valuable information about the importance of each input variable [66]. The first-order and total Sobol indices can be defined as follows:

$$S_i = \frac{\text{Var} [E_{\sim i} [Y|X_i]]}{\text{Var} [Y]} \quad (16)$$

$$S_i^T = \frac{E_{\sim i} [\text{Var} [Y|\mathbf{X}_{\sim i}]]}{\text{Var} [Y]} \quad (17)$$

for a specific value of  $X_i$ , the value of  $Y$  can be determined by averaging the model evaluations over a sample of  $\mathbf{X}_{\sim i}$  while keeping  $X_i = x_i^*$  fixed, where  $\mathbf{X}_{\sim i}$  represents all variables except  $X_i$ .

### D. Kucherenko Indices

Unlike metrics such as Sobol, LIME, and SHAP, the Kucherenko indices accounts for the dependencies among input features. As an extension of the Sobol sensitivity indices, the Kucherenko indices is specifically designed to quantify the sensitivity of model outputs to input variables while considering these interdependencies [63, 66, 82]. The Kucherenko indices essentially involves computing Sobol indices after first employing Copulas [83] (typically Gaussian Copulas) to separate each feature's marginal distribution from the dependency

structure [84], as detailed in Table S2. This approach approximates the correlated variables as independent before calculating the Sobol indices. The Gaussian copula is constructed based on the standard normal distribution, and its mathematical expression is:

$$C(u_1, u_2, \dots, u_d; \Sigma) = \Phi_{\Sigma} [\Phi^{-1}(u_1), \Phi^{-1}(u_2), \dots, \Phi^{-1}(u_d)] \quad (18)$$

where  $u_i = F_i(x_i)$  is the Cumulative Distribution Function (CDF) of the marginal distribution,  $\Phi^{-1}$  is the inverse of the CDF of the standard normal distribution  $\mathcal{N}(0, 1)$ ,  $\Phi_{\Sigma}$  is the CDF of a multivariate normal distribution with mean zero and covariance matrix  $\Sigma$ , and  $\Sigma$  is the correlation matrix, describing the dependence structure between the random variables.

### E. Dataset construction & feature preprocessing

The dataset used in this work is sourced from the aflowlib.org database [85], comprising a total of 5,578 entries. For feature selection, the focus was primarily on characteristics related to vibrational, thermodynamic, and mechanical properties at room temperature (300K), which are theoretically associated with LTC according to first-principles researches [86, 87]. For more details, please refer to Table II. In the modeling aimed at LTC, the model predicts the logarithm of  $\kappa$  ( $\log(\kappa)$ ) rather than the LTC itself. This is because the logarithmic transformation compresses the target value space, thereby enhancing the performance of the ML models [88]. For deep models such as MLPs and KANs, normalization of features is essential as these models rely on gradient descent for parameter optimization. Normalization enhances numerical stability by ensuring that features with different ranges contribute equally to the gradient computations; otherwise, features with larger values might dominate the optimization process [89]. However, this step is unnecessary for XGBoost [90], as it is based on decision trees. Additionally, for interpretability reasons, feature normalization is often omitted in recent works based on SISSO [26, 28, 91]. In this work, we employed Min-Max Normalization, which is expressed as:

$$x' = \frac{x - x_{\min}}{x_{\max} - x_{\min}} \quad (19)$$

where  $x$  is the original feature value,  $x_{\min}$  and  $x_{\max}$  are the minimum and maximum values of the feature, respectively, and  $x'$  is the normalized feature value.

### F. Implementation of DFT & GPUMD methods

DFT and AIMD calculations are performed using VASP [92, 93]. The Projector-Augmented Wave (PAW) method [94] and the Perdew-Burke-Ernzerhof (PBE) functional [95] within the Generalized Gradient Approximation (GGA) are employed for electron exchange-correlation. The cutoff energy is set to 500 eV, and the electronic convergence threshold is  $10^{-8}$  eV.

For the calculation of LTC, both the phonon Boltzmann Transport Equation (BTE) method and Molecular Dynamics

(MD) simulations are used. For the stable  $\text{Be}_2\text{C}$  structure, specific heat and LTC are computed using ShengBTE [96]. The force constants are generated with Hiphive [97]. For other structures, specific heat is calculated using Phonopy [98], while LTC is determined through GPUMD [99]. AIMD-NVT simulations are carried out in the canonical ensemble (NVT) with a Nosé–Hoover thermostat at 300 K for a duration of 5 ns. Uniformly spaced sampling is performed, with 250 frames extracted to train the NEP model. The HNEMD method is employed in GPUMD simulations. A  $\text{Fe}$  value of  $1 \times 10^{-4} \text{ \AA}^{-1}$  has been tested and found to be optimal for this study.

### G. Data Availability

The original LTC data and the selected features can be downloaded from <https://aflowlib.org/> or accessed via the GitHub homepage at <https://github.com/FlorianTseng/LTC-modeling>.

### H. Code Availability

The codes supporting our research are available at <https://github.com/FlorianTseng/LTC-modeling>.

### I. Declaration of competing interest

The authors declare that they have no known competing financial interests or personal relationships that could have appeared to influence the work reported in this paper.

## ACKNOWLEDGMENTS

We would like to acknowledge the National Key R&D Program of China (Grant No. 2023YFB4603800), the financial support from the project of the National Natural Science Foundation of China (Grants No.12404062, No.12474093, No.12302220, No.12374091), Translational Medicine and Interdisciplinary Research Joint Fund of Zhongnan Hospital of Wuhan University (Grant NO.ZNJC202235), and the Fundamental Research Funds for the Central Universities (Grant No.2042023kf0109). The numerical calculations in this work have been done on the supercomputing system in the Supercomputing Center of Wuhan University.

SUPPLEMENTARY INFORMATION

**Supplementary Note 1. KAN's symbolic model on complete dataset**

The simplified symbolic model in the main text Eq.(5), derived from key physical features, is sufficient for an accurate description of LTC. However, for reference, we also provide the symbolic expression fitted by KAN using the complete dataset. It is worth noting that, due to the architecture of KAN, this formula is inevitably more complex. Therefore, we present it solely in its Python representation:

```

1     log(kappa) =
2     4.78*(0.01*atan(7.93*\gamma - 3.22) - 0.02*atanh(1.65*F - 1.02) - 1 + 0.05*exp(-100.0*(-\
    Theta - 0.04)**2) - 0.03*exp(-92.16*(-C_v - 0.06)**2) - 0.02*exp(-40.96*(-C_p - 0.06)
    **2) + 0.02*exp(-2.9*(0.22 - K_{i})**2) - 0.02*exp(-38.44*(0.07 - S_v)**2) - 0.04*exp
    (-60.69*\alpha**2)**4 - 0.16*tanh(-0.26*sin(5.58*SG + 6.4) + 0.53*tan(1.34*F - 9.54)
    + 0.69*tanh(7.9*C_p - 2.41) + 0.5*tanh(10.0*C_v - 3.2) + 0.32*Abs(9.94*S_v - 0.82) +
    0.86*atan(4.61*K_{s} - 1.72) + 0.29 - 81.47*exp(-100.0*(-\alpha - 0.16)**2) + 2.09*exp
    (-100.0*(-\Theta - 0.08)**2) + 0.17*exp(-100.0*(0.54 - \gamma)**2) - 1.45*exp
    (-14.44*(0.12 - K_{i})**2) - 0.08*tanh(2.45*tan(1.08*F - 0.8) + 1.27*tan(1.77*K_{i} -
    0.76) + 0.95*tan(1.87*K_{s} - 0.84) + 0.78*tan(1.77*S_v + 2.4) + 0.03*tan(3.17*\Theta
    + 1.57) + 0.37*tanh(4.25*SG - 2.9) - 1.15 - 0.66*exp(-43.72*(0.27 - \gamma)**2) -
    0.32*exp(-100.0*(0.24 - \alpha)**2) + 0.67*exp(-100.0*(0.02 - C_p)**2) + 0.72*exp
    (-100.0*C_v**2) - 0.07*Abs(0.22*sin(10.0*\gamma + 1.0) - 0.75*tan(2.34*K_{s} - 0.97)
    + 0.34*tanh(10.0*F - 4.9) - 0.34*atan(10.0*\Theta - 0.6) + 0.37*atanh(2.6*C_p - 0.95)
    + 1.52 - 0.27*exp(-8.1*(0.41 - SG)**2) + 0.42*exp(-49.0*(0.2 - S_v)**2) - 0.92*exp
    (-100.0*(0.14 - \alpha)**2) + 0.42*exp(-100.0*(0.13 - K_{i})**2) - 0.93*exp
    (-81.0*(0.07 - C_v)**2) - 4.57 - 0.21*exp(-1.86*(-0.03*tan(3.11*K_{s} - 7.81) - 0.02*
    tan(3.4*SG + 4.4) - 0.14*tan(4.26*\alpha + 7.97) - 0.12*Abs(7.59*\Theta - 1.03) -
    0.18*atan(7.53*\gamma - 4.87) + 0.16*atanh(2.0*F - 1.08) - 0.08 + exp(-2.56*(-K_{i} -
    0.03)**2) + 0.28*exp(-88.36*(0.09 - S_v)**2) - 0.16*exp(-100.0*(0.04 - C_v)**2) -
    0.23*exp(-100.0*(0.04 - C_p)**2)**2) - 0.53*exp(-12.72*(0.04*sin(5.04*SG + 2.18) +
    0.11*tan(2.64*K_{s} + 4.81) - 0.08*tan(2.77*\Theta - 4.58) + 0.32*tanh(9.0*\alpha -
    0.44) - 0.1*tanh(10.0*\gamma - 6.6) - 0.34*atan(2.52*F - 1.63) + 0.15*atan(9.0*S_v -
    1.56) + 0.04*sign(2.64 - 10.0*C_p) - 1 - 0.43*exp(-21.25*(-K_{i} - 0.1)**2) + 0.11*exp
    (-81.0*(0.15 - C_v)**2)**2) + 0.04*exp(-10.71*(0.17*sin(6.2*C_p - 0.15) + 0.12*atan
    (5.2*S_v - 3.27) + 0.04*sign(4.06 - 9.4*\gamma) + 0.03*sign(9.0 - 10.0*SG) - 1 + 0.97*
    exp(-96.04*(-\alpha - 0.07)**2) - 0.65*exp(-100.0*(-C_v - 0.06)**2) - 0.41*exp
    (-11.5*(0.95 - \Theta)**2) - 0.21*exp(-5.76*(0.38 - F)**2) + 0.44*exp(-3.24*(0.14 - K_{
    s})**2) + 0.62*exp(-1.96*(0.05 - K_{i})**2)**2)

```

**Supplementary Note 2. Multi-Layer Perceptrons (MLPs)**

The theoretical framework of MLPs is well-established. Therefore, in this work, we emphasize the distinctions between MLPs and KANs. Unlike KANs, MLPs are founded on the universal approximation theorem [100], which can be mathematically expressed as:

$$f(x) \approx \sum_{i=1}^N \alpha_i \sigma(\omega_i^T x + b_i) \quad (\text{Supplementary Eq.1})$$

where  $\alpha$  are the coefficients,  $\sigma$  is the activation function (we adopted ReLU [101] in this work),  $\omega_i$  and  $b_i$  denote the weights and biases,  $N$  represents the number of neurons in the hidden layer. The expression of MLPs can be simplified to:

$$\text{MLP}(\mathbf{x}) = (\mathbf{W}_{L-1} \circ \sigma \circ \mathbf{W}_{L-1} \circ \sigma \circ \dots \circ \mathbf{W}_1 \circ \sigma \circ \mathbf{W}_0) \mathbf{x} \quad (\text{Supplementary Eq.2})$$

In MLPs, only the weights and biases, which serve as linear parameters, are learnable, while the nonlinear activation functions are fixed as hyperparameters.

### Supplementary Note 3. eXtreme Gradient Boost (XGB)

XGB represents a great advancement over the traditional Gradient Boosting Decision Tree (GBDT) algorithm. Its innovations include the incorporation of regularization to enhance generalization, a two-step gradient approximation of the objective function to accelerate computational efficiency, column subsampling to mitigate noise and further bolster generalization, and an advanced method for handling missing values by assigning a default classification direction at tree nodes, which renders it particularly effective for sparse datasets [102]. GBDT algorithms, including XGB, are computationally intensive particularly in tasks with high-dimensional features and large datasets [102, 103].

### Supplementary Note 4. Crystal Graph Convolutional Neural Network (CGCNN)

CGCNN [104] directly learns from the connection of atoms in a crystal, representing the crystal as a graph with atoms as nodes and bonds as edges. This graph-based approach enables the model to automatically extract optimal representations for predicting material properties. The key feature of CGCNN is its Convolutional Neural Network (CNN) built on top of these crystal graphs. The convolutional layers update the feature vectors of atoms by incorporating information from neighboring atoms and bonds, using the following graph convolution function:

$$v_i^{(t+1)} = \text{Conv} \left( v_i^{(t)}, v_j^{(t)}, u_{(i,j)}^{(k)} \right), (i, j)_k \in G \quad (\text{Supplementary Eq.3})$$

where  $v_i^{(t)}$  is the feature vector of atom  $i$  at layer  $t$ , and  $u_{(i,j)}^{(k)}$  is the feature vector of the bond between atoms  $i$  and  $j$ . After multiple convolutional layers, the pooling layers aggregate the atomic feature vectors into an overall crystal representation, which is then passed to fully connected layers to predict material properties.

### Supplementary Note 5. SHAP Indices

Shapley Additive Explanations (SHAP) [105] is derived from the concept of Shapley values [106] in game theory, which were originally employed to assess the contribution of each individual player to the collective gain within a coalition [107]. Shapley value for individual player can be expressed as:

$$\phi_i = \sum_{S \subseteq N \setminus \{i\}} \frac{|S|! (|N| - |S| - 1)!}{|N|!} (v(S \cup \{i\}) - v(S)), \quad i = 1, 2, \dots, N \quad (\text{Supplementary Eq.4})$$

where  $N$  represents the set of all features,  $S$  is any subset of features that does not include feature  $i$ ,  $|S|$  is the number of features in set  $S$ ,  $v(S)$  is the contribution of feature set  $S$  to the model's prediction output, and  $(S \cup \{i\})$  is the contribution of the feature set  $S \cup \{i\}$ , which includes feature  $i$ , to the model's prediction output. The core concept of SHAP is to generate explanations for individual predictions, which can then be aggregated to provide both local and global insights into the model's behavior [105], it can be expressed mathematically as:

$$\hat{f}(\mathbf{x}) = \phi_0 + \sum_{i=1}^N \phi_i(\mathbf{x}) \quad (\text{Supplementary Eq.5})$$

where  $\phi_i(\mathbf{x})$  is the Shapley value of the  $i$ -th variable,  $\phi_0$  is typically set as the expected value of the training samples,  $\hat{f}(\mathbf{x})$  represents the original prediction made by the model [108].

### Supplementary Note 6. LIME Indices

Local Interpretable Model-agnostic Explanations (LIME) [60] is a perturbation-based method for feature importance analysis that employs a local surrogate model to interpret individual samples. By generating perturbations around the selected sample, a new dataset is created, and an interpretable model (such as linear regression) is trained. The difference between the two models is then measured using an objective function:

$$\xi(x) = \arg \min_{g \in G} L(f, g, \pi_x) + \Omega(g) \quad (\text{Supplementary Eq.6})$$

in the expression,  $f$  denotes the model to be explained,  $g$  represents a simplified model drawn from a set  $G$  of potential models (such as linear models),  $\pi_x$  quantifies the distance between new samples  $x'$  and the original samples  $x$ , and  $\Omega(g)$  reflects the complexity of the model  $g$ .

### Supplementary Note 7. Supplementary Tables

Supplementary Table 2. Marginal distribution of individual primary features determined by Copula sampling.

	Distribution	Parameters
$\Theta$	lognorm	$\mu = -1.935, \sigma = 0.519$
$\gamma$	lognorm	$\mu = 1.671, \sigma = 0.012$
$C_p$	lognorm	$\mu = -2.611, \sigma = 0.778$
$C_v$	lognorm	$\mu = -2.674, \sigma = 0.831$
$\alpha$	lognorm	$\mu = -2.370, \sigma = 0.507$
$S_v$	norm	$\mu = 0.323, \sigma = 0.119$
$F$	lognorm	$\mu = -0.027, \sigma = 0.102$
$K_s$	gamma	$k = 2.546, \theta = 0.102$
$K_i$	gamma	$k = 2.441, \theta = 0.104$

### Supplementary Note 8. Supplementary Figure

The variables involved in Table S2 are classified into three types of distributions: Gamma distribution, normal distribution, and log-normal distribution. Their respective probability density functions (PDF) can be expressed as:

$$f(x) = \frac{1}{\Gamma(k)\theta^k} x^{k-1} e^{-\frac{x}{\theta}}, \quad (\text{Supplementary Eq.7})$$

$$f(x) = \frac{1}{\sqrt{2\pi}\sigma^2} \exp\left(-\frac{(x-\mu)^2}{2\sigma^2}\right), \quad (\text{Supplementary Eq.8})$$

$$f(x) = \frac{1}{x\sigma\sqrt{2\pi}} e^{-\frac{[\ln(x)-\mu]^2}{2\sigma^2}}. \quad (\text{Supplementary Eq.9})$$

- 
- [1] Weixiong Wu, Guoqing Zhang, Xiufang Ke, Xiaoqing Yang, Ziyuan Wang, and Chenzhen Liu. Preparation and thermal conductivity enhancement of composite phase change materials for electronic thermal management. *Energy conversion and management*, 101:278–284, 2015.
  - [2] Qifeng Zhang, Evan Uchaker, Stephanie L Candelaria, and Guozhong Cao. Nanomaterials for energy conversion and storage. *Chemical Society Reviews*, 42(7):3127–3171, 2013.
  - [3] Xiaowei Liu and Ziyu Wang. Printable thermoelectric materials and applications. *Frontiers in Materials*, 6:88, 2019.
  - [4] Çağıl Köroğlu and Eric Pop. High thermal conductivity insulators for thermal management in 3d integrated circuits. *IEEE Electron Device Letters*, 44(3):496–499, 2023.
  - [5] Hussam Jouhara, Alina Zabnieńska Góra, Navid Khordehghah, Qusay Doraghi, Lujean Ahmad, Les Norman, Brian Axcell, Luiz Wrobel, and Sheng Dai. Thermoelectric generator (teg) technologies and applications. *International Journal of Thermofluids*, 9:100063, 2021.
  - [6] Zahid Maqbool, M Hanief, and Malik Parveez. Review on performance enhancement of phase change material based heat sinks in conjugation with thermal conductivity enhancers for electronic cooling. *Journal of Energy Storage*, 60:106591, 2023.
  - [7] O Altun, Y Erhan Boke, and A Kalemantas. Problems for determining the thermal conductivity of tbc's by laser-flash method. *Journal of Achievements in materials and manufacturing engineering*, 30(2):115–120, 2008.
  - [8] Adam A Wilson, Miguel Muñoz Rojo, Begoña Abad, Jaime Andrés Perez, Jon Maiz, Jason Schomacker, Marisol Martín-Gonzalez, Diana-Andra Borca-Tasciuc, and Theodorian Borca-Tasciuc. Thermal conductivity measurements of high and low thermal conductivity films using a scanning hot probe method in the  $3\omega$  mode and novel calibration strategies. *Nanoscale*, 7(37):15404–15412, 2015.
  - [9] David A Broido, Michael Malorny, Gerd Birner, Natalio Mingo, and DA Stewart. Intrinsic lattice thermal conductivity of semiconductors from first principles. *Applied Physics Letters*, 91(23), 2007.
  - [10] Aleksandr Chernatynskiy and Simon R Phillpot. Evaluation of computational techniques for solving the boltzmann transport equation for lattice thermal conductivity calculations. *Physical Review B—Condensed Matter and Materials Physics*, 82(13):134301, 2010.
  - [11] Zheyong Fan, Luiz Felipe C Pereira, Hui-Qiong Wang, Jin-Cheng Zheng, Davide Donadio, and Ari Harju. Force and heat current formulas for many-body potentials in molecular dynamics simulations with applications to thermal conductivity calculations. *Physical Review B*, 92(9):094301, 2015.

- [12] Yufeng Luo, Mengke Li, Hongmei Yuan, Huijun Liu, and Ying Fang. Predicting lattice thermal conductivity via machine learning: a mini review. *npj Computational Materials*, 9(1):4, 2023.
- [13] Keith T Butler, Daniel W Davies, Hugh Cartwright, Olexandr Isayev, and Aron Walsh. Machine learning for molecular and materials science. *Nature*, 559(7715):547–555, 2018.
- [14] Ankit Agrawal and Alok Choudhary. Perspective: Materials informatics and big data: Realization of the “fourth paradigm” of science in materials science. *Apl Materials*, 4(5), 2016.
- [15] Juan J de Pablo, Nicholas E Jackson, Michael A Webb, Long-Qing Chen, Joel E Moore, Dane Morgan, Ryan Jacobs, Tresa Pollock, Darrell G Schlom, and Eric S Toberer. New frontiers for the materials genome initiative. *npj Computational Materials*, 5(1):41, 2019.
- [16] Siwar Chibani and François-Xavier Coudert. Machine learning approaches for the prediction of materials properties. *Apl Materials*, 8(8), 2020.
- [17] Jie Gong, Sharon Chu, Rohan K Mehta, and Alan JH McGaughey. Xgboost model for electrocaloric temperature change prediction in ceramics. *npj Computational Materials*, 8(1):140, 2022.
- [18] Ghanshyam Paliana, Chenchen Wang, Xun Jiang, Sanguthevar Rajasekaran, and Ramamurthy Ramprasad. Accelerating materials property predictions using machine learning. *Scientific Reports*, 3(1):2810, 2013.
- [19] Ghanshyam Paliana. Machine learning in materials science: From explainable predictions to autonomous design. *Computational Materials Science*, 193:110360, 2021.
- [20] Jesús Carrete, Wu Li, Natalio Mingo, Shidong Wang, and Stefano Curtarolo. Finding unprecedentedly low-thermal-conductivity half-heusler semiconductors via high-throughput materials modeling. *Physical Review X*, 4(1):011019, 2014.
- [21] Lihua Chen, Huan Tran, Rohit Batra, Chiho Kim, and Rampi Ramprasad. Machine learning models for the lattice thermal conductivity prediction of inorganic materials. *Computational Materials Science*, 170:109155, 2019.
- [22] Xinming Wang, Shuming Zeng, Zhuchi Wang, and Jun Ni. Identification of crystalline materials with ultra-low thermal conductivity based on machine learning study. *The Journal of Physical Chemistry C*, 124(16):8488–8495, 2020.
- [23] Christian Loftis, Kunpeng Yuan, Yong Zhao, Ming Hu, and Jianjun Hu. Lattice thermal conductivity prediction using symbolic regression and machine learning. *The Journal of Physical Chemistry A*, 125(1):435–450, 2020.
- [24] Diogo V Carvalho, Eduardo M Pereira, and Jaime S Cardoso. Machine learning interpretability: A survey on methods and metrics. *Electronics*, 8(8):832, 2019.
- [25] Leilani H Gilpin, David Bau, Ben Z Yuan, Ayesha Bajwa, Michael Specter, and Lalana Kagal. Explaining explanations: An overview of interpretability of machine learning. In *2018 IEEE 5th International Conference on data science and advanced analytics (DSAA)*, pages 80–89. IEEE.
- [26] Runhai Ouyang, Stefano Curtarolo, Emre Ahmetcik, Matthias Scheffler, and Luca M Ghiringhelli. Sisso: A compressed-sensing method for identifying the best low-dimensional descriptor in an immensity of offered candidates. *Physical Review Materials*, 2(8):083802, 2018.
- [27] Glen A Slack. Nonmetallic crystals with high thermal conductivity. *Journal of Physics and Chemistry of Solids*, 34(2):321–335, 1973.
- [28] Thomas AR Purcell, Matthias Scheffler, Luca M Ghiringhelli, and Christian Carbogno. Accelerating materials-space exploration for thermal insulators by mapping materials properties via artificial intelligence. *npj computational materials*, 9(1):112, 2023.
- [29] Yuqin Xu and Quan Qian. i-ssiso: Mutual information-based improved sure independent screening and sparsifying operator algorithm. *Engineering Applications of Artificial Intelligence*, 116:105442, 2022.
- [30] Ziming Liu, Yixuan Wang, Sachin Vaidya, Fabian Ruehle, James Halverson, Marin Soljačić, Thomas Y Hou, and Max Tegmark. Kan: Kolmogorov-arnold networks. *arXiv preprint arXiv:2404.19756*, 2024.
- [31] Yuntian Hou, Jinheng Wu, and Xiaohang Feng. A comprehensive survey on kolmogorov arnold networks (kan). *arXiv preprint arXiv:2407.11075*, 2024.
- [32] Kunpeng Xu, Lifei Chen, and Shengrui Wang. Kolmogorov-arnold networks for time series: Bridging predictive power and interpretability. *arXiv preprint arXiv:2406.02496*, 2024.
- [33] Mohd Herwan Sulaiman, Zuriani Mustafa, Muhammad Salihin Saealal, Mohd Mawardi Saari, and Abu Zaharin Ahmad. Utilizing the kolmogorov-arnold networks for chiller energy consumption prediction in commercial building. *Journal of Building Engineering*, page 110475, 2024.
- [34] Hao Liu, Jin Lei, and Zhongzhou Ren. From complexity to clarity: Kolmogorov-arnold networks in nuclear binding energy prediction. *arXiv preprint arXiv:2407.20737*, 2024.
- [35] Tian Xie and Jeffrey C Grossman. Crystal graph convolutional neural networks for an accurate and interpretable prediction of material properties. *Physical review letters*, 120(14):145301, 2018.
- [36] Zhen Hua Wang, Yun Fei Liu, Tao Wang, Jian Guo Wang, Yuan Ming Liu, and Qing Xue Huang. Intelligent prediction model of mechanical properties of ultrathin niobium strips based on xgboost ensemble learning algorithm. *Computational Materials Science*, 231:112579, 2024.
- [37] Tianqi Chen and Carlos Guestrin. Xgboost: A scalable tree boosting system. In *Proceedings of the 22nd acm sigkdd international conference on knowledge discovery and data mining*, pages 785–794.
- [38] Eiji Mizutani and Stuart E Dreyfus. On complexity analysis of supervised mlp-learning for algorithmic comparisons. In *IJCNN’01. International Joint Conference on Neural Networks. Proceedings (Cat. No. 01CH37222)*, volume 1, pages 347–352. IEEE.
- [39] Adam Paszke, Sam Gross, Francisco Massa, Adam Lerer, James Bradbury, Gregory Chanan, Trevor Killeen, Zeming Lin, Natalia Gimelshein, and Luca Antiga. Pytorch: An imperative style, high-performance deep learning library. *Advances in neural information processing systems*, 32, 2019.
- [40] Fabian Pedregosa, Gaël Varoquaux, Alexandre Gramfort, Vincent Michel, Bertrand Thirion, Olivier Grisel, Mathieu Blondel, Peter Prettenhofer, Ron Weiss, and Vincent Dubourg. Scikit-learn: Machine learning in python. *the Journal of machine Learning research*, 12:2825–2830, 2011.

- [41] Takuya Akiba, Shotaro Sano, Toshihiko Yanase, Takeru Ohta, and Masanori Koyama. Optuna: A next-generation hyperparameter optimization framework. In *Proceedings of the 25th ACM SIGKDD international conference on knowledge discovery & data mining*, pages 2623–2631.
- [42] Lei Xu. Machine learning problems from optimization perspective. *Journal of Global Optimization*, 47:369–401, 2010.
- [43] Davide Chicco, Matthijs J Warrens, and Giuseppe Jurman. The coefficient of determination r-squared is more informative than smape, mae, mape, mse and rmse in regression analysis evaluation. *Peerj computer science*, 7:e623, 2021.
- [44] Cuixin Ma, Wei-Li Liu, Jinghui Zhong, and Liang Feng. Comparison analysis on techniques of preprocessing imbalanced data for symbolic regression. In *CCF Conference on Computer Supported Cooperative Work and Social Computing*, pages 256–270. Springer.
- [45] Ekaterina Vladislavleva, Guido Smits, and Dick Den Hertog. On the importance of data balancing for symbolic regression. *IEEE Transactions on Evolutionary Computation*, 14(2):252–277, 2009.
- [46] Yuxiang Gao, Yi Zhu, and Yu Zhao. Dealing with imbalanced data for interpretable defect prediction. *Information and software technology*, 151:107016, 2022.
- [47] Henry Han, Yi Wu, Jiacun Wang, and Ashley Han. Interpretable machine learning assessment. *Neurocomputing*, 561:126891, 2023.
- [48] Leo Grinsztajn, Edouard Oyallon, and Gaël Varoquaux. Why do tree-based models still outperform deep learning on typical tabular data? *Advances in neural information processing systems*, 35:507–520, 2022.
- [49] Jun Xia, Lecheng Zhang, Xiao Zhu, Yue Liu, Zhangyang Gao, Bozhen Hu, Cheng Tan, Jiangbin Zheng, Siyuan Li, and Stan Z Li. Understanding the limitations of deep models for molecular property prediction: Insights and solutions. *Advances in Neural Information Processing Systems*, 36, 2024.
- [50] DA Broido, A Ward, and N Mingo. Lattice thermal conductivity of silicon from empirical interatomic potentials. *Physical Review B—Condensed Matter and Materials Physics*, 72(1):014308, 2005.
- [51] Julius Ranninger. Lattice thermal conductivity. *Physical Review*, 140(6A):A2031, 1965.
- [52] Kelsy Cabello-Solorzano, Isabela Ortigosa de Araujo, Marco Pena, Luís Correia, and Antonio J. Tallon-Ballesteros. The impact of data normalization on the accuracy of machine learning algorithms: a comparative analysis. In *International Conference on Soft Computing Models in Industrial and Environmental Applications*, pages 344–353. Springer.
- [53] Philip B. Allen. Anharmonic phonon quasiparticle theory of zero-point and thermal shifts in insulators: Heat capacity, bulk modulus, and thermal expansion. *Physical Review B*, 92(6):064106, 2015. PRB.
- [54] Rafael M Digilov and Haim Abramovich. Temperature variation of the isothermal bulk modulus in solids: Thermo-elastic instability and melting. *Journal of Applied Physics*, 125(6), 2019.
- [55] Yan Feng, Dong Huang, and Wei Li. Adiabatic bulk modulus of elasticity for 2d liquid dusty plasmas. *Physics of Plasmas*, 25(5), 2018.
- [56] Haohua Wen and CH Woo. Quantum statistical vibrational entropy and enthalpy of formation of helium-vacancy complex in bcc w. *Journal of Nuclear Materials*, 482:99–104, 2016.
- [57] Animesh Pan, Tanmoy Kar, Animesh K Rakshit, and Satya P Moulik. Enthalpy-entropy compensation (eec) effect: decisive role of free energy. *The Journal of Physical Chemistry B*, 120(40):10531–10539, 2016.
- [58] GD Garbulsky and G Ceder. Contribution of the vibrational free energy to phase stability in substitutional alloys: Methods and trends. *Physical Review B*, 53(14):8993, 1996.
- [59] Scott Lundberg and Su In Lee. A unified approach to interpreting model predictions. In *Nips*.
- [60] Marco Tulio Ribeiro, Sameer Singh, and Carlos Guestrin. "why should i trust you?": Explaining the predictions of any classifier, 2016.
- [61] Andrew Gelman. Analysis of variance—why it is more important than ever. *The Annals of Statistics*, 33(1):1–53, 53, 2005.
- [62] Nhu Cuong Do and Saman Razavi. Correlation effects? a major but often neglected component in sensitivity and uncertainty analysis. *Water Resources Research*, 56(3):e2019WR025436, 2020.
- [63] Sergei Kucherenko, Stefano Tarantola, and Paola Annoni. Estimation of global sensitivity indices for models with dependent variables. *Computer physics communications*, 183(4):937–946, 2012.
- [64] Stefano Marelli and Bruno Sudret. *UQLab: A framework for uncertainty quantification in Matlab*, pages 2554–2563. 2014.
- [65] Laura Toloşi and Thomas Lengauer. Classification with correlated features: unreliability of feature ranking and solutions. *Bioinformatics*, 27(14):1986–1994, 2011.
- [66] Philippe Wiederkehr. *Global sensitivity analysis with dependent inputs*. Thesis, 2018.
- [67] Logan Ward, Alexander Dunn, Alireza Faghaninia, Nils ER Zimmermann, Saurabh Bajaj, Qi Wang, Joseph Montoya, Jiming Chen, Kyle Bystrom, and Maxwell Dylla. Matminer: An open source toolkit for materials data mining. *Computational Materials Science*, 152:60–69, 2018.
- [68] Lauri Himanen, Marc OJ Jäger, Eiaki V Morooka, Filippo Federici Canova, Yashasvi S Ranawat, David Z Gao, Patrick Rinke, and Adam S Foster. Dscribe: Library of descriptors for machine learning in materials science. *Computer Physics Communications*, 247:106949, 2020.
- [69] Jinlong Hu, Yuting Zuo, Yuzhou Hao, Guoyu Shu, Yang Wang, Minxuan Feng, Xuejie Li, Xiaoying Wang, Jun Sun, and Xiangdong Ding. Prediction of lattice thermal conductivity with two-stage interpretable machine learning. *Chinese Physics B*, 32(4):046301, 2023.
- [70] Zihao Yang, Xixin Wu, Xindang He, and Xiaofei Guan. A multiscale analysis-assisted two-stage reduced-order deep learning approach for effective thermal conductivity of arbitrary contrast heterogeneous materials. *Engineering Applications of Artificial Intelligence*, 136:108916, 2024.
- [71] A Jain, SP Ong, G Hautier, W Chen, WD Richards, S Dacek, S Cholia, D Gunter, D Skinner, and G Ceder. The materials project: a materials genome approach to accelerating materials innovation. *apl mater* 1: 011002, 2013.
- [72] Xu Liu, Xi Jiang, Tong Wang, Zhen Zhang, and Zhao Liu. Lattice thermal conductivity of two-dimensional crb4 and mob4 monolayers against slack’s guideline. *Results in Physics*, 51:106696, 2023.
- [73] V Maurya, U Paliwal, G Sharma, and KB Joshi. Thermoelectric and vibrational properties of be 2 c, bemgc and mg 2 c using first-principles method. *RSC advances*, 9(24):13515–13526, 2019.

- [74] Huimin Wang, Guangzhao Qin, Zhenzhen Qin, Guojian Li, Qiang Wang, and Ming Hu. Lone-pair electrons do not necessarily lead to low lattice thermal conductivity: an exception of two-dimensional penta-cn<sub>2</sub>. *The Journal of Physical Chemistry Letters*, 9(10):2474–2483, 2018.
- [75] Zhonghua Yang, Wenbo Ning, Alejandro Rodriguez, Lihua Lu, Junxiang Wang, Yagang Yao, Kunpeng Yuan, and Ming Hu. Anti-bonding mediated record low and comparable-to-air lattice thermal conductivity of two metallic crystals. *Journal of Materials Chemistry C*, 11(44):15657–15668, 2023.
- [76] Shuming Zeng, Qian Shen, Lei Fang, Zonglin Gu, Jinpeng Yang, Geng Li, Yusong Tu, and Jun Ni. Room temperature high thermoelectric performance of bi-based full-heusler compounds csxb3-xbi with strong anharmonicity. *International Journal of Heat and Mass Transfer*, 217:124628, 2023.
- [77] Qi Zhong, Zhenhong Dai, Weiqiang Wang, Yinchang Zhao, and Sheng Meng. Quartic anharmonicity and ultra-low lattice thermal conductivity of alkali antimonide compounds m<sub>3</sub>sb (m= k, rb and cs). *International Journal of Energy Research*, 45(5):6958–6965, 2021.
- [78] Yuzhe Yang, Kaiwen Zha, Yingcong Chen, Hao Wang, and Dina Katabi. Delving into deep imbalanced regression. In *International conference on machine learning*, pages 11842–11851. PMLR, 2023.
- [79] Andrei Nikolaevich Kolmogorov. On the representation of continuous functions of many variables by superposition of continuous functions of one variable and addition. In *Doklady Akademii Nauk*, volume 114, pages 953–956. Russian Academy of Sciences, 1937.
- [80] Johannes Schmidt-Hieber. The kolmogorov-arnold representation theorem revisited. *Neural networks*, 137:119–126, 2021.
- [81] Jianqing Fan and Jinchu Lv. Sure independence screening for ultra-high dimensional feature space. *Journal of the Royal Statistical Society*, 70(5):849–911, 2006.
- [82] M Munoz Zuniga, S Kucherenko, and Nilay Shah. Metamodeling with independent and dependent inputs. *Computer Physics Communications*, 184(6):1570–1580, 2013.
- [83] Roger B Nelsen. *An introduction to copulas*. Springer, 2006.
- [84] David Lopez-Paz, Jose Miguel Hernández-Lobato, and Ghahramani Zoubin. Gaussian process vine copulas for multivariate dependence. In *International Conference on Machine Learning*, pages 10–18. PMLR, 2016.
- [85] Stefano Curtarolo, Wahyu Setyawan, Gus LW Hart, Michal Jahnatek, Roman V Chepulskii, Richard H Taylor, Shidong Wang, Junkai Xue, Kesong Yang, and Ohad Levy. Aflow: An automatic framework for high-throughput materials discovery. *Computational Materials Science*, 58:218–226, 2012.
- [86] Xudong Zhang and Wei Jiang. First-principles investigations on vibrational, thermodynamic, mechanical properties and thermal conductivity of 112 al<sub>3</sub>x (x= sc, er, tm, yb) intermetallics. *Physica Scripta*, 90(6):065701, 2015.
- [87] Yu Zhou, Yan Cheng, Xiang-Rong Chen, Cui-E Hu, and Qi-Feng Chen. First-principles investigations on elastic, thermodynamic and lattice thermal conductivity of topological insulator laas. *Philosophical Magazine*, 98(20):1900–1918, 2018.
- [88] Monika Berendt-Marchel and A Wawrzynczak. Does the zero carry essential information for artificial neural network learning to simulate the contaminant transport in urban areas? In *Journal of Physics: Conference Series*, volume 2090, page 012027. IOP Publishing, 2019.
- [89] Dalwinder Singh and Birmohan Singh. Investigating the impact of data normalization on classification performance. *Applied Soft Computing*, 97:105524, 2020.
- [90] Elias Amancio Siqueira-Filho, Maira Farias Andrade Lira, Attilio Converti, Hugo Valadares Siqueira, and Carmelo JA Bastos-Filho. Predicting thermoelectric power plants diesel/heavy fuel oil engine fuel consumption using univariate forecasting and xgboost machine learning models. *Energies*, 16(7):2942, 2023.
- [91] Anran Wei, Han Ye, Zhenlin Guo, and Jie Xiong. Sisso-assisted prediction and design of mechanical properties of porous graphene with a uniform nanopore array. *Nanoscale advances*, 4(5):1455–1463, 2022.
- [92] G. Kresse and J. Furthmüller. Efficiency of ab-initio total energy calculations for metals and semiconductors using a plane-wave basis set. *Computational Materials Science*, 6(1):15–50, 1996.
- [93] G. Kresse and J. Furthmüller. Efficient iterative schemes for ab initio total-energy calculations using a plane-wave basis set. *Physical Review B*, 54(16):11169–11186, 1996. PRB.
- [94] Jens Jorgen Mortensen, Lars Bruno Hansen, and Karsten Wedel Jacobsen. Real-space grid implementation of the projector augmented wave method. *Physical Review B—Condensed Matter and Materials Physics*, 71(3):035109, 2005.
- [95] John P Perdew, Kieron Burke, and Matthias Ernzerhof. Generalized gradient approximation made simple. *Physical review letters*, 77(18):3865, 1996.
- [96] Wu Li, Jesús Carrete, Nebil A. Katcho, and Natalio Mingo. Shengbte: A solver of the boltzmann transport equation for phonons. *Computer Physics Communications*, 185(6):1747–1758, 2014.
- [97] Fredrik Eriksson, Erik Fransson, and Paul Erhart. The hiphive package for the extraction of high-order force constants by machine learning. *Advanced Theory and Simulations*, 2(5):1800184, 2019.
- [98] Atsushi Togo, Laurent Chaput, Terumasa Tadano, and Isao Tanaka. Implementation strategies in phonopy and phono3py. *Journal of Physics: Condensed Matter*, 35(35):353001, 2023.
- [99] Zheyong Fan, Wei Chen, Ville Vierimaa, and Ari Harju. Efficient molecular dynamics simulations with many-body potentials on graphics processing units. *Computer Physics Communications*, 218:10–16, 2017.
- [100] George Cybenko. Approximation by superpositions of a sigmoidal function. *Mathematics of control, signals and systems*, 2(4):303–314, 1989.
- [101] Abien Fred M. Agarap. Deep learning using rectified linear units (relu). 2018.
- [102] Tianqi Chen and Carlos Guestrin. Xgboost: A scalable tree boosting system. In *Proceedings of the 22nd acm sigkdd international conference on knowledge discovery and data mining*, pages 785–794. ACM, 2016.
- [103] Chang Yu, Yixin Jin, Qianwen Xing, Ye Zhang, Shaobo Guo, and Shuchen Meng. Advanced user credit risk prediction model using lightgbm, xgboost and tabnet with smoteenn. *arXiv preprint arXiv:2408.03497*, 2024.

- [104] Tian Xie and Jeffrey C Grossman. Crystal graph convolutional neural networks for an accurate and interpretable prediction of material properties. *Physical review letters*, 120(14):145301, 2018.
- [105] Scott Lundberg and Su In Lee. A unified approach to interpreting model predictions. In *Nips*.
- [106] Joanna Roder, Laura Maguire, Robert Georgantas, and Heinrich Roder. Explaining multivariate molecular diagnostic tests via shapley values. *BMC Medical Informatics and Decision Making*, 21(1):211, 2021.
- [107] L. S. Shapley. A value for n-person games. *Contributions to the Theory of Games*, 1953.
- [108] Pramudita Satria Palar, Yohanes Bimo Dwianto, Lavi Rizki Zuhul, Joseph Morlier, Koji Shimoyama, and Shigeru Obayashi. Multi-objective design space exploration using explainable surrogate models. *Structural and Multidisciplinary Optimization*, 67(3):38, 2024.